

How Small Is Too Small for the Capillarity Theory?

Alexandre B. Almeida, Sergey V. Buldyrev, Adriano M. Alencar, and Nicolas Giovambattista*



Cite This: *J. Phys. Chem. C* 2021, 125, 5335–5348



Read Online

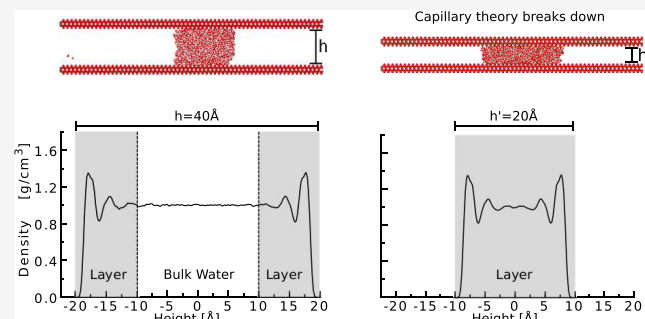
ACCESS |

Metrics & More

Article Recommendations

Supporting Information

ABSTRACT: We perform molecular dynamics (MD) simulations of nanoscale water capillary bridges (WCBs) expanding between two parallel walls and determine the smallest separation between the walls above which the capillarity theory (CT) remains valid. We consider silica-based walls with tuned surface partial charges that expand from hydrophobic to hydrophilic. We find that the CT is valid (i.e., it predicts successfully the WCB geometry and forces induced on the walls) for, approximately, wall separations $h \geq h_0 = 3.0$ nm for all surfaces considered. At these separations, the CT holds without including any line tension and the results are robust relative to the method employed to obtain the WCB profile from MD simulations. At approximately $2.0 \text{ nm} \leq h < h_0$, the contact angle of water θ varies with h , suggesting that at such wall separations the CT requires the inclusion of a line tension τ . However, we find that the specific behavior of $\theta(h)$ and the associated value of τ are inherently dependent on the method employed to calculate the WCB profile from MD simulations. Interestingly, the forces induced by the WCBs on the walls obey the prediction of the CT without the need to include a line tension for approximately $h \geq 2.5$ nm for all surfaces considered. Our results are interpreted in terms of the rearrangement of water molecules within the WCBs and show that the CT breaks down at $h < h_0$ because its assumptions, that the WCB is a bulklike water volume confined by solid–liquid and liquid–vapor interfaces, do not hold.



I. INTRODUCTION

Capillarity is the study of deformable interfaces formed between a liquid and a vapor or between immiscible liquids.¹ Examples of capillarity phenomenon include the formation of droplets on a surface and the rise of a liquid within a narrow space (e.g., a thin tube) without the assistance of, or even in opposition to, external forces such as gravity. The capillarity theory (CT) is well-established^{1,2} (the Young–Laplace equation is more than 200 years old^{3,4}) and has been applied extensively to explain diverse phenomena, from the locomotion of insects on a water surface⁵ to the transfer of ink processes via capillary bridges in dip-pen nanolithography.⁶ The CT is a macroscopic theory where liquids are treated as a continuum. However, as the systems under study become smaller, within the nanometer scale, such an approximation is expected to break down. Indeed, numerous experimental and computational studies indicate that at the nanometer scale, the molecular nature of liquids cannot be avoided (see, e.g., refs 7, 8). Not surprisingly, the study of capillarity at nanometer scales remains an active field of research.⁹

A natural question follows: what is the smallest length scale at which the CT, as originally formulated, remains valid? In this work, we address this question by studying water capillary bridges (WCBs) expanding between two identical flat surfaces that range from hydrophobic (water contact angle $\theta > 90^\circ$) to hydrophilic ($\theta < 90^\circ$). Our study is based on molecular dynamics (MD) simulations of realistic models of water and

confining walls (silica). In our previous studies,^{10,11} we showed that the CT successfully predicts the geometric (capillary bridge profile, contact angles, average surface curvature, etc.) and thermodynamic properties (e.g., capillary forces induced on the confining surfaces) of nanoscale water capillary bridges (WCBs) expanding between homogeneous surfaces separated by “large” distances, $h \geq 50$ Å. Similar results were obtained in the case of more complex heterogeneous surfaces, composed of a hydrophilic patch on a hydrophobic background.^{12,13} Interestingly, we found that the CT can also predict the thermodynamic limit of stability of such capillary bridges¹¹ as a function of h , at large wall separations ($h > 50$ Å). In this work, we focus on homogenous hydrophobic and hydrophilic surfaces and test whether the CT can also predict the properties of WCBs at very ‘small’ wall separations, $h = 15–50$ Å. As $h \rightarrow 0$, the WCB acquires a pancake-like shape sandwiched between the confining walls and, hence, the confining dimension h becomes relevant. This represents a fundamental difference from our previous studies,^{10,11} since, in the limit $h \rightarrow 0$, the role of the solid–liquid–vapor line tension

Received: December 14, 2020

Revised: February 13, 2021

Published: March 2, 2021



cannot be avoided and should be studied in detail. Moreover, it is expected that for very small wall separations, water molecules within the WCBs arrange into layers parallel to the walls.^{14–16} Indeed, atomic force microscopy (AFM) experiments and computer simulations clearly show that such a layering effect is responsible for the oscillatory forces observed in AFM experiments as the atomic force microscope tip moves away from the sample of interest.^{7,17–19}

We note that capillary bridges in general, and WCBs in particular, play an important role in scientific and technological applications. For example, capillary forces exerted by liquid bridges provide a major contribution to the tensile strength of soils^{20,21} and represent the primary source of cohesive forces in granular materials²² and nanoparticles.^{7,23} WCBs can form naturally between the tip of an atomic force microscope and the substrate under study depending on the relative humidity of the environment.^{24,25} In these cases, capillary forces can affect the AFM measurements.^{17,19} Capillary bridges are important in surface science in general, e.g., WCBs can induce adhesion and/or friction^{26,27} between the interacting surfaces. Interestingly, capillary bridges are relevant for the physiology of the lung.^{28,29}

This paper is organized as follows. In **Section II**, we describe the computational details. The results are presented in **Section III** where we discuss the ability of the CT to predict the geometric and thermodynamic properties of the WCB as determined from MD simulations. We also explore how the hypothesis of the CT is affected as the wall separation decreases. A summary and discussion are included in **Section IV**.

II. METHODS

We perform MD simulations of an axisymmetric WCB expanding between two identical hydrophilic/hydrophobic silica walls; see **Figures 1** and **2**. We employ the same

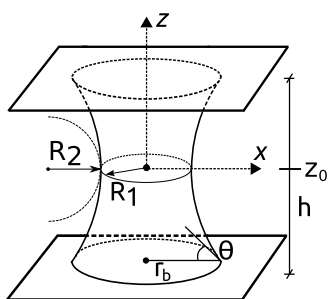


Figure 1. Schematic diagram of the capillary bridges studied in this work with the corresponding relevant parameters. R_1 and R_2 are the first and second radii of curvature of the liquid–vapor interface, respectively; the average curvature of the interface is $H = (1/R_1 + 1/R_2)/2$ and has the same value at every point of the liquid–vapor interface. r_b is the radius of the capillary bridge's base (in contact with the walls), and θ is the contact angle of water. h and z_0 are, respectively, the capillary bridge height and neck position ($z_0 = 0$). Adopted from ref 11.

computational techniques and numerical methods used in our previous studies; see refs 10, 11 for details. Briefly, the walls are perpendicular to the z -axis and are located at $z = \pm h/2$, where h is the wall–wall distance. The walls expand across the simulation box and have a side length $L = 277.2$ Å; the simulation box is cubic with a side length L . In the present study, the walls are four times larger than those employed in

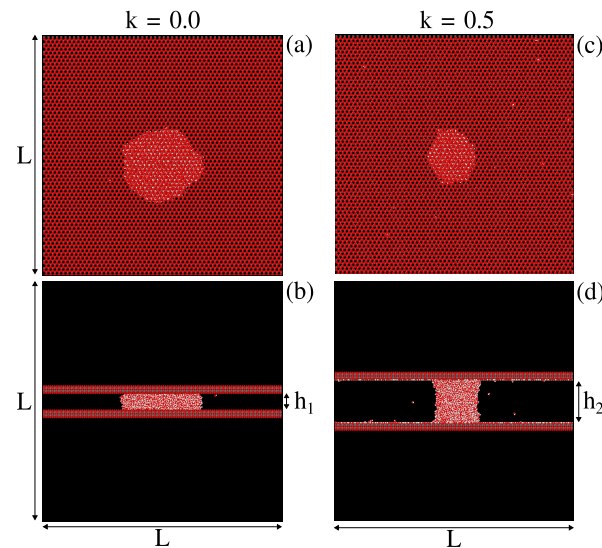


Figure 2. Snapshots of a water capillary bridge expanding between (a), (b) two hydrophobic (nonhydroxylated silica, $k = 0.0$) and (c), (d) two hydrophilic walls (hydroxylated silica, $k = 0.5$). Upper and lower rows show the top and side views of the corresponding capillary bridges. The wall separations are $h_1 = 20$ Å (left column) and $h_2 = 50$ Å (right column); the wall side length is $L = 277.2$ Å, same as the simulation box side length.

ref 11. Simulations are performed at a constant number of water molecules $N = 3375$, volume V , and temperature $T = 300$ K. All computer simulations are performed using the LAMMPS software package,³⁰ and we use the Nosé–Hoover style thermostat to keep the temperature constant. Electrostatic interactions are calculated using the particle–particle particle–mesh solver³¹ with a cutoff distance of $r_{\text{cutoff}} = 10.0$ Å. The same cutoff distance is used to calculate the Lennard-Jones (LJ) interactions.

The water molecules are represented using the SPC/E model,³² and the silica walls are described in detail in ref 14. Briefly, the walls are composed of four layers of SiO_2 (β -cristobalite). The wall atoms have no partial charges and the walls are effectively hydrophobic with (SPC/E) water contact angle of $\approx 108^\circ$, see ref 36 (Figure 1a,b). The silica walls are made hydrophilic by adding a H atom to the Si–O groups of the wall surface facing the capillary bridge; see Figure 2c,d. These surfaces are hydrophilic due to partial charges $q_{0,\text{Si}} = 0.31e$, $q_{0,\text{O}} = -0.71e$, and $q_{0,\text{H}} = 0.4e$ located on the Si–O–H atoms of the silanol groups, which make the surface polar.¹⁴ To generate a family of polar surfaces, we rescale the Si–O–H partial charges by a constant k , i.e., $q_i \rightarrow k \times q_{0,i}$, where $i = \text{Si}, \text{O}$, and H .³⁶ The resulting silica walls are hydrophilic (hydrophobic) for surface polarity $k > 0.346$ ($k < 0.346$). Since the H atoms have no LJ interactions, setting $k = 0.0$ effectively removes the wall H atoms. It follows that for $k = 0.0$, the walls reduce to the hydrophobic silica walls defined above (Figure 2a,b).

The Si and O atoms are located at fixed positions during the whole simulation while the H atoms of the surface silanol groups are able to rotate in a circle parallel to the walls. The wall separation h is defined by the distance between the planes containing the H atoms of each wall. In the case of hydrophobic walls ($k = 0.0$), h is defined by the distance between the planes containing the surface O atoms of each wall.

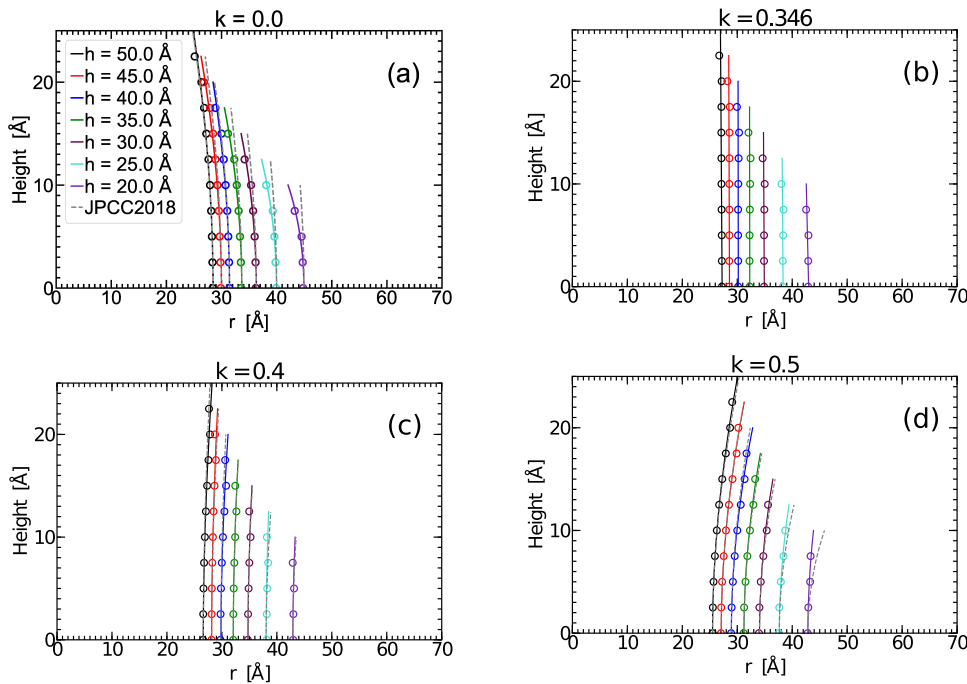


Figure 3. Average profile of the water capillary bridges formed between walls for selected surface polarity k and wall separations h (average bridge profiles for other values of k and h are included in Figure S1 of the Supporting Information). Circles represent the capillary bridge profiles obtained from MD simulations using slabs of thickness $\delta_s = 5 \text{ \AA}$ and located every $\delta_z = \delta_s/2 = 2.5 \text{ \AA}$; see the text. The solid lines are the theoretical profiles based on eq 1 that fit the MD data; the corresponding fitting parameters are given in Tables 1 and 2. The dashed gray lines are the theoretical profiles obtained when the contact angles in Tables 1 and 2 are substituted by the contact angles that we reported in ref 11 obtained for $h \geq 50 \text{ \AA}$. Dashed lines in (a) and (d) deviate from the MD profile (circles), indicating that the contact angles calculated at $h \geq 50 \text{ \AA}$ do not necessarily apply as $h \rightarrow 20 \text{ \AA}$.

Our simulations are performed at $T = 300 \text{ K}$ and relative humidity that varies depending of the interface curvature, so the vapor and liquid phases are always at equilibrium. At these conditions only about 5 molecules are expected to be found in the vapor phase and about 10 molecules absorbed to the walls, even at the largest polarities studied. Since our simulations are done at constant number of molecules, the humidity of the environment does not play any role in our idealized simulations. In AFM experiments the variations of relative humidity of the environment can cause extra water molecules to be absorbed on the walls, modifying the contact angle of water and contributing to additional forces between the surfaces.^{33–35}

A series of MD simulations are performed sequentially with decreasing wall separations, $h = 50, 45, 40, \dots, 20 \text{ \AA}$. At each h , we run a simulation for $\Delta t_{\text{sim}} = 3 \text{ ns}$. We find that the resulting compression rate $\Delta h/\Delta t_{\text{sim}}$ is sufficiently slow and the compression process of the AS bridge can be considered quasi-static (the thermalization of the AS bridge at a given h is very fast; e.g., the average forces on the walls become constant in less than 100 ps). The change in wall separation, $h \rightarrow h' = h - 5 \text{ \AA}$, is performed via a set of short 250 fs simulations, in which each wall is displaced by 0.01 \AA every 1 fs. Simulations at $h < 20 \text{ \AA}$ are performed following a similar procedure but in smaller steps, $h = 19, 18, 17, \dots, 15 \text{ \AA}$. During the simulations at a given h , the configurations of water molecules and the forces on each wall are saved every 1 ps. Only the last 2 ns of the simulated time interval Δt_{sim} are used for data analysis.

III. RESULTS AND DISCUSSION

The results are separated into three sections. In Section III.I, we discuss the geometrical properties of the WCB, including the capillary bridge profile and the water contact angle. In particular, we compare the WCB profiles obtained from MD simulations and the CT. In Section III.II, we study the role played by the (liquid–vapor–solid) line tension in the CT. In Section III.III, we study the forces induced by the WCB on the walls. Section III.IV focuses on the density profile of water along the WCB and explores whether the hypotheses of the CT apply at different wall separations.

III.I. Geometrical Properties of Water Capillary Bridges.

Figure 3 shows the average profile of the WCB for selected hydrophobic/hydrophilic surfaces with different surface polarities and for wall separations in the range of $20.0 \leq h \leq 50.0 \text{ \AA}$ (additional average profiles for different values of k and h are included in Figure S1 of the Supporting Information). The circles indicate the average WCB profiles obtained from MD simulations, $r_{\text{MD}}(z)$. As explained in detail in our previous studies,^{10,11} to calculate $r_{\text{MD}}(z)$, we divide the WCB in slabs of thickness $\delta_s = 5 \text{ \AA}$ parallel to the walls. For each slab centered at height z , we calculate the corresponding water density as a function of r , where r is the radial distance to the axis perpendicular to the walls that passes through the center of mass of the WCB. The radius of the WCB at height z , $r_{\text{MD}}(z)$, is defined as the radial distance at which the density of water within the slab drops from $\approx 1 \text{ g/cm}^3$ at $\rho \approx 1 \text{ g/cm}^3$ at $r \approx 0$ to $\rho \approx 0.2 \text{ g/cm}^3$ at $r_{\text{MD}}(z)$. In Figure 3, the slabs are centered at $z = -(h/2-2.5), -(h/2-5.0), \dots, 0.0, \dots, (h/2-5.0), (h/2-2.5) \text{ \AA}$, i.e., the slabs are located every $\delta_z = \delta_s/2 = 2.5 \text{ \AA}$ and, hence, they partially overlap.

Table 1. Parameters Obtained by Fitting the WCB Profiles Obtained from MD Simulations, Shown in Figures 3 and S1 of the Supporting Information (Circles), Using Equation 1^a

$k = 0.0$					$k = 0.1$					
h	r_0 (Å)	R_2 (Å)	H (Å ⁻¹)	θ (deg)	ϵ (Å)	r_0 (Å)	R_2 (Å)	H (Å ⁻¹)	θ (deg)	ϵ (Å)
50.0	28.5	86.4	0.0233	105.3	0.053	28.2	93.2	0.0231	104.1	0.037
45.0	30.0	69.9	0.0238	107.8	0.046	29.6	79.8	0.0231	105.4	0.035
40.0	31.4	69.0	0.0231	106.4	0.047	31.2	72.4	0.0229	105.5	0.038
35.0	33.7	51.1	0.0246	109.9	0.052	33.2	65.3	0.0227	105.4	0.039
30.0	36.3	43.2	0.0253	110.5	0.061	35.8	51.7	0.0236	107.0	0.049
25.0	40.0	30.9	0.0287	114.4	0.065	39.2	38.8	0.0256	109.1	0.045
20.0	45.0	19.4	0.0369	122.0	0.079	44.0	24.8	0.0315	114.4	0.052
$k = 0.2$					$k = 0.3$					
h	r_0 (Å)	R_2 (Å)	H (Å ⁻¹)	θ (deg)	ϵ (Å)	r_0 (Å)	R_2 (Å)	H (Å ⁻¹)	θ (deg)	ϵ (Å)
50.0	28.0	113.2	0.0222	101.5	0.036	27.4	289.9	0.02	94.4	0.042
45.0	29.2	127.1	0.0211	99.5	0.041	28.9	262.5	0.0192	94.6	0.053
40.0	31.0	98.7	0.0212	101.3	0.04	30.6	186.9	0.019	95.9	0.037
35.0	33.0	80.4	0.0213	102.4	0.045	32.6	177.0	0.0182	95.6	0.048
30.0	35.4	75.7	0.0207	101.4	0.044	35.3	120.1	0.0183	97.2	0.054
25.0	38.8	53.3	0.0223	103.8	0.051	38.5	80.8	0.0192	99.0	0.045
20.0	43.7	30.2	0.028	109.8	0.054	43.3	51.0	0.0214	101.5	0.042

^aSurface polarities are $k = 0.0, 0.1, 0.2, and 0.3 (see also Table 2). R_1 ($r_0 = R_1$) and R_2 are the radii of curvature of the water capillary bridge's neck; see Figure 1. $H = \frac{1}{2} \left(\frac{1}{R_1} + \frac{1}{R_2} \right)$ is the average surface curvature of the capillary bridge, θ is the corresponding contact angle of water, and ϵ is the error of the theoretical profile.³⁹ Errors in r_0 and R_2 are ± 0.05 Å.$

Table 2. Same as Table 1 for the Theoretical Profiles of Figures 3 and S1 of the Supporting Information Corresponding to Surface Polarities $k = 0.346, 0.4$, and 0.5

$k = 0.346$					$k = 0.4$					
h	r_0 (Å)	R_2 (Å)	H (Å ⁻¹)	θ (deg)	ϵ (Å)	r_0 (Å)	R_2 (Å)	H (Å ⁻¹)	θ (deg)	ϵ (Å)
50.0	27.2	∞	0.0184	90.7	0.031	26.6	-186.0	0.0161	83.4	0.036
45.0	28.6	∞	0.0175	90.3	0.038	28.1	-231.3	0.0156	85.0	0.031
40.0	30.2	∞	0.0166	90.1	0.037	29.8	-154.3	0.0135	83.1	0.044
35.0	32.3	∞	0.0155	90.1	0.042	32.1	-177.4	0.0128	84.5	0.045
30.0	34.9	∞	0.0143	90.6	0.044	34.8	-162.2	0.0113	84.8	0.054
25.0	38.3	∞	0.013	90.8	0.054	38.0	-182.3	0.0104	86.0	0.061
20.0	43.0	∞	0.0116	92.5	0.062	42.9	-127.4	0.0077	85.4	0.075
$k = 0.5$					r_0 (Å)	R_2 (Å)	H (Å ⁻¹)	θ (deg)	ϵ (Å)	
h	r_0 (Å)	R_2 (Å)	H (Å ⁻¹)	θ (deg)	r_0 (Å)	R_2 (Å)	H (Å ⁻¹)	θ (deg)	ϵ (Å)	
50.0	25.5	-64.8	0.0119	71.5						
45.0	27.1	-58.7	0.01	70.7						
40.0	28.9	-51.3	0.0075	69.5						
35.0	31.2	-51.9	0.0064	71.7						
30.0	34.0	-47.3	0.0041	72.3						
25.0	37.6	-45.8	0.0024	74.4						
20.0	42.8	-51.1	0.0019	78.7						

The solid lines in Figure 3 are the theoretical profiles that fit $r_{MD}(z)$. Specifically, the CT predicts that the profile of the WCB is given by²⁸

$$\frac{dz}{dr} = \pm \frac{|H(r^2 - r_0^2) + r_0|}{\sqrt{r^2 - [H(r^2 - r_0^2) + r_0]^2}} \quad (1)$$

where $r(z)$ is the radius of the WCB at height z . The plus (minus) sign applies to the case $z > 0$ ($z < 0$), where $z = 0$ is the position of the WCB neck; see Figure 1. r_0 is the radius of the WCB at $z = 0$. The solid lines in Figure 3 are obtained using eq 1 and the corresponding fitting parameters are given in Tables 1 and 2.

The contact angles resulting from the theoretical profiles (solid lines) in Figure 3 are shown in Figure 4a,b as a function of h (see also Tables 1 and 2). It follows that for all surfaces studied, $\theta(h)$ remains constant for approximately $h > 30$ Å, but it varies with the wall separations for approximately $h \leq 30$ Å. At $30 < h \leq 50$ Å, the contact angles are in agreement with the contact angles reported in our previous studies^{10,11,36} obtained for $h \geq 50$ Å; see Figure 4c. Interestingly, the behavior of $\theta(h)$ over the whole range of wall separations studied, $20 \leq h \leq 75$ Å, can be approximated by

$$\cos \theta(h) = a/h^2 + b/h + \cos \theta_\infty \quad (2)$$

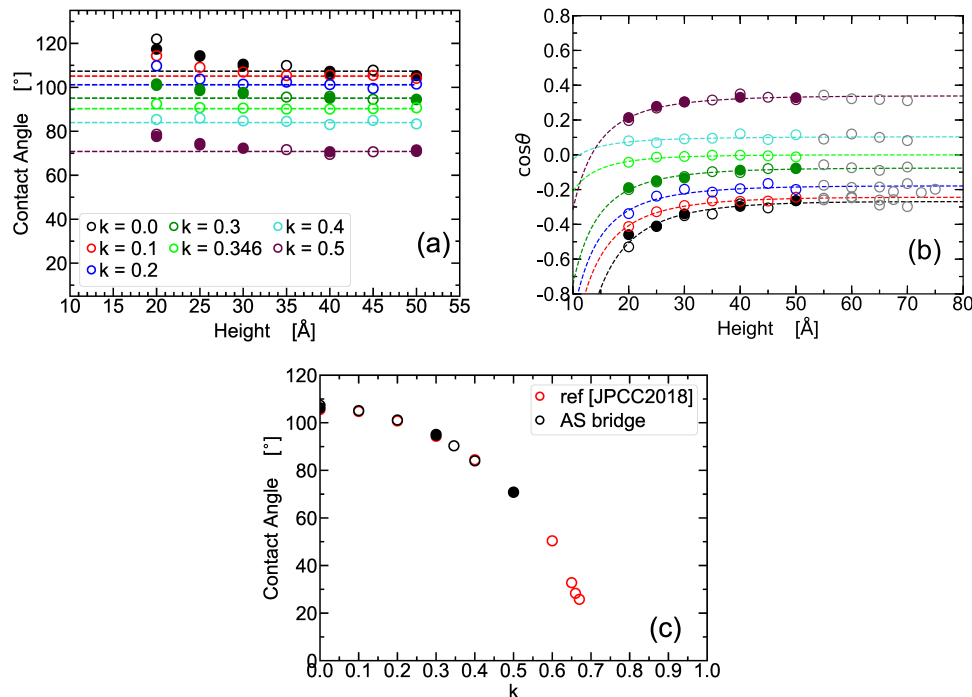


Figure 4. (a) Water contact angle $\theta(h)$ obtained from the capillary bridges formed between walls of surface polarities k separated by a distance h . Values of $\theta(h)$ are calculated from the solid lines in Figures 3 and S1 of the Supporting Information (see also Tables 1 and 2). The dashed lines indicate the contact angles averaged over $h > 30 \text{ \AA}$. (b) Cosine of the contact angles shown in (a). Gray circles are the values of $\cos\theta(h)$ obtained in ref 11 for $h > 50 \text{ \AA}$. The dashed lines are the best fit using the equation $\cos\theta(h) = a/h^2 + b/h + \cos\theta_\infty$; parameters a , b , and $\cos\theta_\infty$ are given in Table 3. (c) Average contact angles obtained from (a) at $30 < h \leq 50 \text{ \AA}$ plotted as a function of the surface polarity k (black circles). For comparison, we include the average contact angles from ref 11 (for $h \geq 50 \text{ \AA}$; red circles). Error bars are smaller than the symbol sizes. Empty and solid black circles (in all panels) are used to distinguish among independent simulations at the same k and h .

where a and b are fitting parameters that depend on k and θ_∞ is the ‘macroscopic’ contact angle obtained at $h \geq 50 \text{ \AA}$; see Table 3.

Table 3. Fitting Parameters for $\cos\theta$ in Figure 4b Using the Expression $\cos\theta(h) = a/h^2 + b/h + \cos\theta_\infty$ ^a

k	a	b	$\cos\theta_\infty$
0.0	-171.8159	4.4262	-0.2981
0.1	-112.8071	2.7091	-0.2607
0.2	-97.4154	2.3536	-0.1936
0.3	-86.0338	2.0269	-0.0886
0.346	-28.0048	0.7497	-0.0056
0.4	-13.7299	0.0689	0.1047
0.5	-82.7455	1.8313	0.3281

^aUnits of a and b are \AA^2 and \AA , respectively; $\cos\theta_\infty$ has no units.

To confirm that the deviations in $\theta(h)$ for small values of h are indeed relevant, we also include in Figure 3 (gray dashed lines) the theoretical profiles obtained using the same parameters given in Tables 1 and 2 but where the contact angle is replaced by the contact angle reported in ref 11 based on MD simulations at $h \geq 50 \text{ \AA}$. It follows from Figure 3 that for approximately $h \leq 30 \text{ \AA}$, the deviations among the theoretical profiles indicated by the solid and dashed lines are indeed relevant.

At severe confinement, the procedure used to measure the WCB from computer simulations may be important. Accordingly, next, we test whether the results of Figures 3 and 4 are sensitive to the procedure followed to calculate the WCB from the MD simulations. The method that we use to

calculate the WCB profiles from MD simulations is probably the most direct procedure that one could think of. It is the same method that is commonly used to calculate the profile of nanoscale droplets and capillary bridges in MD simulations (see, e.g., refs 17, 19, 37, 38). As explained in Section III.I, our method depends on a single parameter δ_s , which is the thickness of the slabs used to calculate $r_{\text{MD}}(z)$ (the distance δ_z by which consecutive slabs are displaced relative to each other is fixed, $\delta_z = \delta_s/2$). Thus, here, we explore how the results presented in Figures 3 and 4 are affected by varying δ_s . We focus on two kinds of surfaces, one hydrophobic, with $k = 0.0$, and another hydrophilic, with $k = 0.5$. For each surface, we calculate the profiles of the WCB from MD simulations using different values of δ_s in the range of $1.0 \leq \delta_s \leq 12.5 \text{ \AA}$. Unfortunately, for cases where $\delta_s < 5 \text{ \AA}$, the radius of the WCB next to the walls can be underestimated. This is due to an inherent gap of the order of 1 \AA that exists between oxygen atoms of the wall surface and water (such a gap can be observed in the density profiles in Figure 10). Accordingly, when calculating the theoretical WCB profile, one also has to remove one or two data points of the profiles obtained from the MD simulations that are closest to the walls (see, e.g., refs 37, 38). Figures S2 and S3 of the Supporting Information show examples of the WCB profiles from MD simulations obtained for $\delta_s = 1.250, 2.500, 2.857, 3.125, 3.333, 4.167, 5.000, 8.33 \text{ \AA}$ and $h = 20, 25, 50 \text{ \AA}$. Also included in Figures S2 and S3 are the theoretical profiles of the WCB obtained using eq 1 (solid lines). The theoretical profiles in Figures S2 and S3 correspond, respectively, to the cases where one and two points of $r_{\text{MD}}(z)$ closest to the upper and lower surfaces are

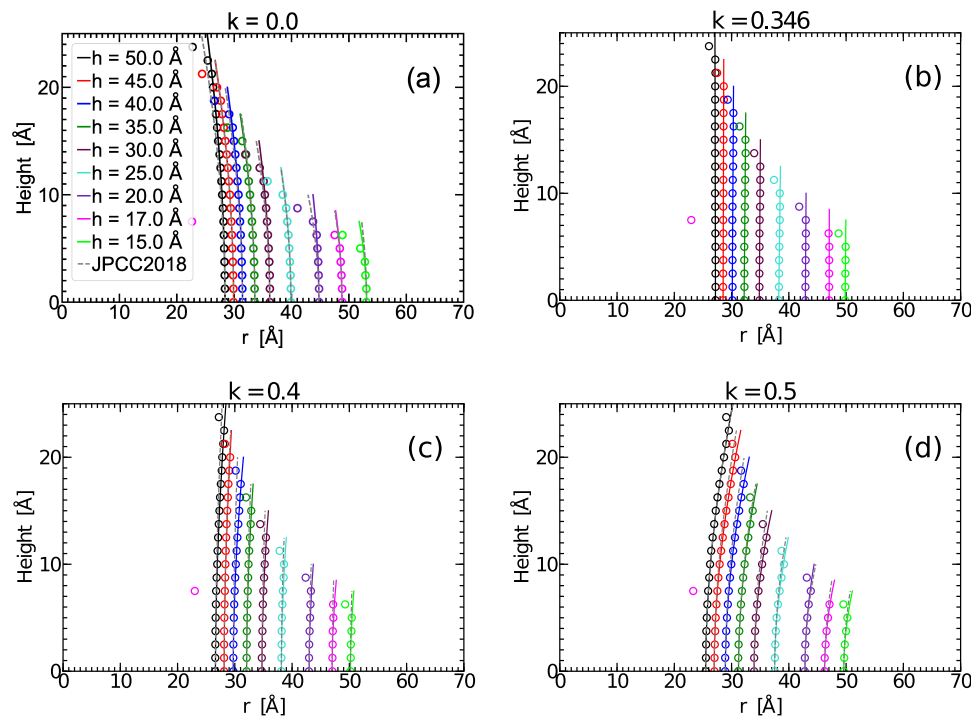


Figure 5. Same as Figure 3 but with the water capillary bridges from MD simulations ($r_{\text{MD}}(z)$, circles) calculated using slabs of thickness $\delta_s = 2.5 \text{ \AA}$ (and located every $\delta_z = \delta_s/2$); see the text. The solid lines are the theoretical profiles based on eq 1 that fit $r_{\text{MD}}(z)$; the corresponding fitting parameters are given in Tables 4 and 5. The dashed gray lines are the theoretical profiles obtained when the contact angles in Tables 4 and 5 are substituted by the contact angles that we reported in ref 11 obtained for $h \geq 50 \text{ \AA}$. Due to the small value of δ_s , the two data points (circles) closest to the upper ($z = h - \delta_z, h - 2\delta_z$) and lower ($z = -(h - \delta_z), -(h - 2\delta_z)$) walls are excluded in the calculation of the theoretical profiles (solid and dashed lines). Additional WCB profiles for other values of k and h are included in Figure S6 of the Supporting Information.

Table 4. Parameters Obtained by Fitting the WCB Profiles Obtained from MD Simulations, Shown in Figures 5 and S6 of the Supporting Information (Circles), Using Equation 1^a

$k = 0.0$						$k = 0.1$				
h	$r_0 (\text{\AA})$	$R_2 (\text{\AA})$	$H (\text{\AA}^{-1})$	$\theta (\text{deg})$	$\epsilon (\text{\AA})$	$r_0 (\text{\AA})$	$R_2 (\text{\AA})$	$H (\text{\AA}^{-1})$	$\theta (\text{deg})$	$\epsilon (\text{\AA})$
50.0	28.4	99.3	0.0226	103.2	0.008	28.2	99.5	0.0227	103.2	0.008
45.0	29.9	79.9	0.023	105.4	0.006	29.6	91.3	0.0224	103.4	0.009
40.0	31.5	77.4	0.0224	104.5	0.009	31.2	80.7	0.0222	103.9	0.006
35.0	33.6	62.2	0.0229	106.2	0.008	33.2	74.5	0.0218	103.4	0.008
30.0	36.2	62.8	0.0218	103.9	0.009	35.7	70.1	0.0211	102.4	0.004
25.0	39.9	47.9	0.023	105.4	0.005	39.2	57.8	0.0214	102.7	0.011
20.0	44.8	51.1	0.021	101.5	0.012	43.9	44.4	0.0227	103.3	0.006
17.0	48.8	34.1	0.0249	104.8	0.012	47.5	37.4	0.0239	103.5	0.011
15.0	53.1	23.5	0.0307	109.1	0.02	50.7	29.6	0.0267	105.1	0.018
$k = 0.2$						$k = 0.3$				
h	$r_0 (\text{\AA})$	$R_2 (\text{\AA})$	$H (\text{\AA}^{-1})$	$\theta (\text{deg})$	$\epsilon (\text{\AA})$	$r_0 (\text{\AA})$	$R_2 (\text{\AA})$	$H (\text{\AA}^{-1})$	$\theta (\text{deg})$	$\epsilon (\text{\AA})$
50.0	27.9	134.1	0.0216	99.6	0.004	27.4	330.2	0.0198	93.9	0.027
45.0	29.2	142.0	0.0206	98.5	0.006	28.8	321.5	0.0189	93.7	0.033
40.0	30.9	128.0	0.0201	98.6	0.008	30.6	229.5	0.0185	94.8	0.019
35.0	33.0	111.1	0.0197	98.9	0.011	32.6	230.6	0.0175	94.3	0.029
30.0	35.4	99.7	0.0191	98.7	0.008	35.3	197.6	0.0167	94.4	0.03
25.0	38.8	75.3	0.0195	99.7	0.016	38.5	102.8	0.0179	97.1	0.029
20.0	43.6	59.1	0.0199	100.0	0.013	43.3	78.9	0.0179	97.5	0.026
17.0	47.2	49.5	0.0207	100.2	0.016	47.4	67.0	0.018	97.5	0.029
15.0	50.6	34.5	0.0244	102.9	0.023	50.5	42.7	0.0216	100.4	0.031

^aSurface polarities are $k = 0.0, 0.1, 0.2$, and 0.3 (see also Table 5). R_1 ($r_0 = R_1$) and R_2 are the radii of curvature of the water capillary bridge's neck; see Figure 1. $H = \frac{1}{2} \left(\frac{1}{R_1} + \frac{1}{R_2} \right)$ is the average surface curvature of the WCB, θ is the corresponding contact angle, and ϵ is the error of the theoretical profiles.³⁹ Errors in r_0 and R_2 are $\pm 0.05 \text{ \AA}$.

Table 5. Same as **Table 4** for the Theoretical Profiles of Figures 5 and S6 of the Supporting Information Corresponding to Surface Polarities $k = 0.346$, 0.4, and 0.5

$k = 0.346$					$k = 0.4$					
h	r_0 (Å)	R_2 (Å)	H (Å $^{-1}$)	θ (deg)	ϵ (Å)	r_0 (Å)	R_2 (Å)	H (Å $^{-1}$)	θ (deg)	ϵ (Å)
50.0	27.2	∞	0.0184	90.2	0.007	26.6	-163.0	0.01572	82.5	0.008
45.0	28.5	∞	0.0175	89.7	0.004	28.1	-195.8	0.01522	84.1	0.012
40.0	30.1	∞	0.0166	89.3	0.011	29.7	-111.9	0.01235	80.5	0.005
35.0	32.2	∞	0.0155	89.1	0.009	32.1	-135.9	0.01192	82.9	0.007
30.0	34.8	∞	0.0144	89.3	0.009	34.7	-102.5	0.00951	81.8	0.013
25.0	38.2	∞	0.0131	88.6	0.004	38.1	-93.7	0.00778	82.3	0.014
20.0	42.9	∞	0.0117	89.3	0.005	43.0	-72.2	0.00471	81.9	0.017
17.0	47.0	∞	0.0106	89.8	0.003	47.0	-52.4	0.00110	80.5	0.017
15.0	49.8	∞	0.01	89.1	0.003	50.2	-50.1	0.00002	81.2	0.011
$k = 0.5$										
h	r_0 (Å)	R_2 (Å)	H (Å $^{-1}$)	θ (deg)	ϵ (Å)					
50.0	25.5	-62.2	0.0116	70.8	0.011					
45.0	27.0	-53.2	0.0091	68.7	0.006					
40.0	28.9	-47.9	0.0069	68.0	0.008					
35.0	31.2	-47.7	0.0055	70.0	0.01					
30.0	33.9	-37.8	0.0015	67.8	0.008					
25.0	37.5	-34.0	-0.0014	69.0	0.008					
20.0	42.8	-32.9	-0.0035	72.4	0.014					
17.0	46.2	-22.3	-0.0116	67.6	0.007					
15.0	49.6	-20.0	-0.0149	67.9	0.01					

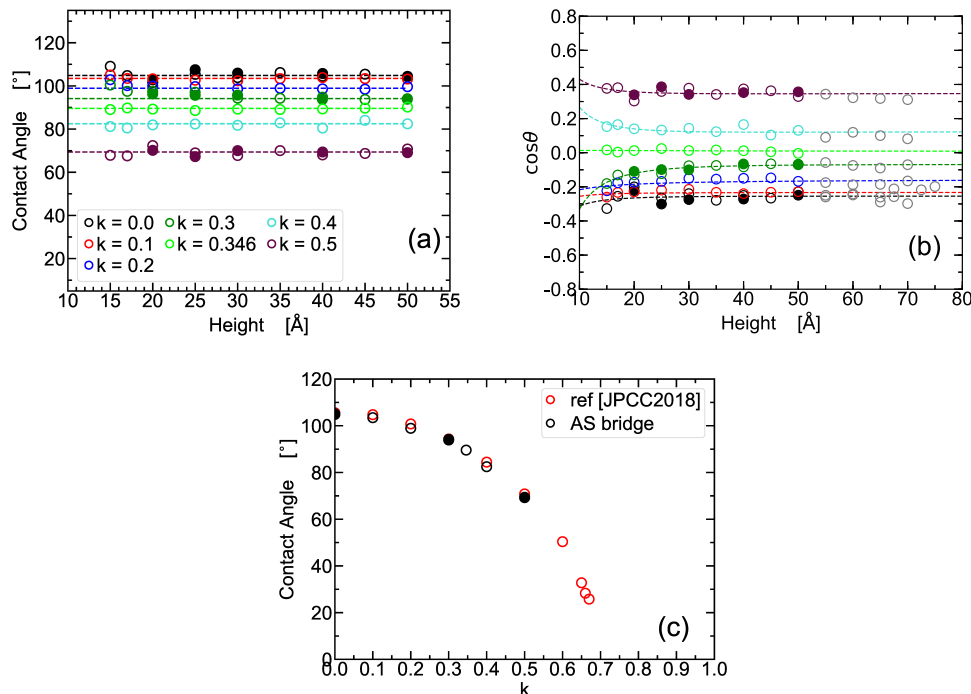


Figure 6. Same as Figure 4 but for the profiles shown in Figures 5 and S6 of the Supporting Information. (a) Water contact angle $\theta(h)$ obtained from theoretical profiles corresponding to the solid lines in Figures 5 and S6 of the Supporting Information (see also Tables 4 and 5). The dashed lines indicate the contact angle averaged over $h > 30$ Å. (b) Cosine of the contact angles shown in (a). The gray circles are the values of $\cos\theta(h)$ obtained in ref 11 for $h \geq 50$ Å. The dashed lines are the best fit using the equation $\cos\theta(h) = a/h_2 + b/h + \cos\theta_\infty$; parameters a , b , and $\cos\theta_\infty$ are given in Table 6. (c) Average contact angle obtained from (a) (for $30 < h \leq 50$ Å; black circles) as a function of the surface polarity k . For comparison, we include the average contact angles from ref 11 (for $h \geq 50$ Å; red circles). Error bars are smaller than the symbol sizes. Empty and solid circles are used to distinguish among independent simulations at the same k and h .

omitted during the fitting procedure followed to obtain the theoretical WCB profiles.

The results from our detailed analysis are summarized in Figures S4 and S5 of the Supporting Information where we show the effects of varying δ_s on θ , H , and the error ϵ between

the theoretical (fitting) and MD profiles³⁹ for selected values of h . If the method employed to obtain the theoretical profiles from the MD simulations is reliable, then θ and H should be independent of δ_s . We find that this is true only for $\delta_s > 2$ Å. In addition, we find that the error³⁹ of the fitting profiles is small,

i.e., $\epsilon \approx O(0.1\text{\AA})$, for $\delta_s > 2\text{--}3\text{\AA}$. Accordingly, we consider the smallest slab thickness δ_s that is suitable to calculate the WCB profile from our MD simulations to be $\delta_s = 2.5\text{\AA}$ ($\epsilon < 0.1\text{\AA}$). This value of δ_s , which is only used to coarse-grain the density of water within the slabs used to calculate $r_{\text{MD}}(z)$, is physically reasonable since it is close to the O–O distance between the nearest water molecules in the bulk, $\approx 2.8\text{\AA}$.

Figure 5 shows profiles of the WCB obtained from MD simulations (circles) using $\delta_s = 2.5\text{\AA}$. The solid lines are the profiles of the WCB obtained from eq 1 when the two points of $r_{\text{MD}}(z)$, closest to the upper and lower walls, are removed (WCB profiles for additional values of h and k are shown in Figure S6 of the Supporting Information; the corresponding fitting parameters are given in Tables 4 and 5). Interestingly, as shown in Figure 6a–c, the contact angles that we obtain at $h < 30\text{\AA}$ are, now, practically independent of h (see also Table 6).

Table 6. Fitting Parameters for $\cos\theta$ in Figure 6b Using the Expression $\cos\theta(h) = a/h^2 + b/h + \cos\theta_\infty$ ^a

k	a	b	$\cos\theta_\infty$
0.0	-7.8488	0.2138	-0.2561
0.1	-2.4229	0.0175	-0.2328
0.2	-0.5387	-0.5665	-0.1550
0.3	-32.3618	0.6469	-0.0725
0.346	-0.9387	0.1514	0.0073
0.4	23.5090	-0.9958	0.1308
0.5	13.9570	-0.6055	0.3519

^aUnits of a and b are \AA ; $\cos\theta_\infty$ has no units.

A comparison of Figures 3 and 4, obtained with $\delta_s = 5\text{\AA}$, with Figures 5 and 6, obtained with $\delta_s = 2.5\text{\AA}$, confirms that (i)

$\cos(\theta)$ is constant for $h \geq 30\text{\AA}$ but it also shows that (ii) the deviations of $\cos(\theta)$ at $h < 30\text{\AA}$ from its constant value at $h \geq 30\text{\AA}$ depend on how the WCB profile is constructed from the MD profiles. In addition, if we fit the WCB profiles obtained from MD simulations in Figure 6 but remove only one point from $r_{\text{MD}}(z)$ closest to the upper and lower walls, we obtain, again, slightly different results. The fitting of the WCB profiles obtained by removal of only one point next to the walls is shown in Figure S7 of the Supporting Information, and the corresponding behavior of $\theta(h)$ is shown in Figure S8. Again, we find that (i) $\cos(\theta)$ is constant for $h \geq 30\text{\AA}$. However, (ii) the deviations of $\cos(\theta)$ at $h < 30\text{\AA}$ from its constant value at $h \geq 30\text{\AA}$ are intermediate from those observed in Figures 4 and 6. We stress that $\delta_s = 2.5$ and 5\AA are equally, physically acceptable values and, hence, there is no reason a priori to choose one against the other. In addition, it is not evident whether one should remove one or two points from $r_{\text{MD}}(z)$ (next to the walls) during the fitting procedure, i.e., there is no universal method to define the liquid–vapor interface from computer simulations³⁸ (at approximately $h < 30\text{\AA}$). Accordingly, our MD simulations suggest that for $h < 30\text{\AA}$, the results from computer simulations are inherently sensitive to the procedure followed to calculate the profile of the WCB.

III.II. Role of the Line Tension. The previous discussion omits possible contributions from the solid–liquid–vapor line tension, τ . This is partially motivated by our previous studies^{10,11} that show that the line tension contributions are not relevant for water nanodroplets and capillary bridges at large wall separations $h \geq 50\text{\AA}$. However, for a WCB of constant volume, the free energy contribution of the liquid–vapor interface decreases as $h \rightarrow 0$ (since the liquid–vapor interface vanishes in this limit), while, instead, the solid–

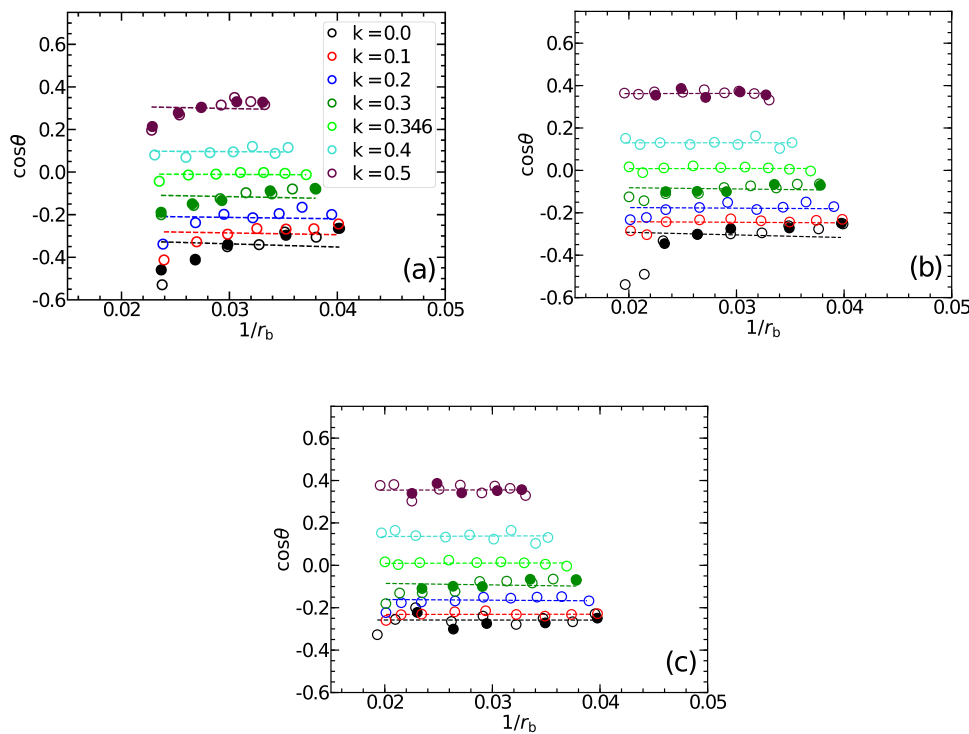


Figure 7. Cosine of water contact angle, $\cos(\theta)$, as a function of the inverse of the WCB base radius, $1/r_b$. (a), (b), and (c) correspond to the data of $\cos(\theta)$ shown in Figures 4b, S8b of the Supporting Information, and Figure 6b. Dashed lines are the fittings obtained using eq 3; fitting parameters are given in Table 7. Open and closed circles are used to distinguish results from independent runs performed at the same conditions (k and h). Error bars are smaller than the symbol sizes.

Table 7. Fitting Parameters for $\cos \theta$ as a Function of $1/r_b$, Shown in Figure 7a–c, Using Equation 3^a

k	Figure 7a		Figure 7b		Figure 7c	
	τ	$\cos \theta_\infty$	τ	$\cos \theta_\infty$	τ	$\cos \theta_\infty$
0.0	-0.00834	-0.292327	-0.00645	-0.267625	0.00011	-0.257545
0.1	-0.00466	-0.260719	-0.00137	-0.237043	0.00028	-0.232826
0.2	-0.00359	-0.193594	-0.00149	-0.169656	-0.00164	-0.155026
0.3	-0.00522	-0.087243	-0.00306	-0.070114	-0.00372	-0.071084
0.346	-0.00104	-0.005556	0.00025	0.007464	0.00053	0.007342
0.4	-0.00162	0.104715	0.00008	0.129788	0.00126	0.130843
0.5	-0.00560	0.328578	0.00053	0.360090	0.00049	0.352844

^aThe values of γ are given in Table 8. Units of τ are 10^{-9} N.

liquid–vapor line contact increases as $h \rightarrow 0$ (since r_b increases in this limit). Therefore, the line tension contribution to the total free energy is expected to be relevant at $h \rightarrow 0$. That τ plays a relevant role in the CT at small wall separations is also suggested by the deviations in $\theta(h)$ at $h \leq 30$ Å from its constant value at $h \geq 30$ Å (although such deviations depend on the method employed to calculate the WCB from the MD simulations). To calculate τ for the different surfaces studied, we note that the effect of including τ on the free energy \mathcal{F} of the WCB is to add the term $\mathcal{F} \rightarrow \mathcal{F} + 2(2\pi r_b)\tau$. As shown in the Supporting Information, minimization of the free energy \mathcal{F} leads to the following relationship between the contact angle of water and the WCB base radius

$$\cos \theta = \cos \theta_\infty - (\tau/\gamma)1/r_b \quad (3)$$

Equation 3 is also valid for droplets and has been confirmed in computer simulations of nanoscale droplets.³⁷

Figure 7a–c shows $\cos(\theta)$ as a function of $1/r_b$ corresponding to Figures 4b and S8b of the Supporting Information, and Figure 6b (circles). The dashed lines are the corresponding fits using eq 3 with the values of θ_∞ fit to the contact angle values obtained for $h \geq 30$ Å (Figures 4c and S8c of the Supporting Information, and Figure 6c). From the slopes of these dashed lines, we obtain the values of τ for the different surfaces considered and for the three different methods employed to calculate the theoretical WCB profile from the MD simulations; see Table 7. It follows from Figure 7a that, for the case $\delta_s = 0.5$ Å, including τ does not explain the variations of $\cos(\theta)$ with $1/r_b$. For the two methods considered where $\delta_s = 2.5$ Å (Figure 7b,c) including τ , apparently explains the variations of the water contact angle with $1/r_b$ (or h). However, as shown in Table 7, the resulting values of τ for a given surface can vary considerably with the method used. This is in contrast with the case of the surface tension γ , the value of which is rather robust, independent on how the theoretical WCB profile is calculated. For example, for $k = 0.0$, τ can be negative (-0.00834×10^{-9} N) or positive (0.00011×10^{-9} N) depending on the method employed. Similarly, for the case $k = 0.5$, τ varies from -0.00560×10^{-9} to 0.00049×10^{-9} N. Accordingly, we conclude that the line tension is an ill-defined quantity at the nanoscale, inherently sensitive to the method used to calculate the WCB from the MD simulations (again, this is in contrast to the case of the surface tension γ). We also note that values of τ are in the range from ≈ -0.008 to 0.001×10^{-9} N, smaller than the values reported in ref 37 for the case of nanodroplets in contact with graphite model surfaces.

III.III. Forces Induced on the Walls. Next, we compare the forces calculated directly from our MD simulations with the corresponding predictions from the CT. Since the value of

τ cannot be defined precisely at $h \leq 30$ Å, we omit the contributions from the line tension to the forces induced on the walls.

The force $F(h)$ that the WCB induces on the walls is a thermodynamic property that can be obtained from the Helmholtz free energy of the system \mathcal{F} . Specifically, thermodynamics states that at constant (N , V , T), $d\mathcal{F} = -dW_{\text{non-PV}}$ where $W_{\text{non-PV}}$ is the external non-PV work done on the system. Since the external force of the system is $F_{\text{ext}} = -F$

$$F = -F_{\text{ext}} = +(\partial\mathcal{F}/\partial h)_{N,T,A} \quad (4)$$

where $A = L \times L$ is the wall surface area. In the case of an axisymmetric capillary bridge and neglecting the contributions from τ

$$\mathcal{F} = \Omega\mathcal{F}_{\text{bulk}} + 2\gamma_{\text{LS}}A_{\text{LS}} + 2\gamma_{\text{SG}}(A - A_{\text{LS}}) + \gamma_{\text{LG}}A_{\text{LG}} + c \quad (5)$$

Here, γ_{LG} , γ_{LS} , and γ_{GS} are, respectively, the liquid–gas, liquid–solid, and gas–solid surface tensions and A_{LG} , A_{LS} , and A_{GS} are the corresponding interfacial surface areas ($A = A_{\text{LS}} + A_{\text{GS}}$). Ω is the volume of the WCB and $\mathcal{F}_{\text{bulk}}$ is the free energy of bulk water per unit volume at the working conditions; Ω and $\mathcal{F}_{\text{bulk}}$ can be considered to be constant at our working conditions. c is an arbitrary constant.

It can be shown²⁸ that for $\theta < 90^\circ$, \mathcal{F} can be expressed in terms of elliptic integrals²⁸ that depend solely on Ω , h , and θ

$$\mathcal{F} = \pi\gamma h^2 \frac{2\sigma(a, 1) - \cos(\theta)}{2u(a, 1)^2} \quad (6)$$

where $u(a, 1)$ and $\sigma(a, 1)$ are elliptic integrals given by eqs A25 and A26 of ref 28, $a = r_0/r_b$. In addition, it follows from eqs 4 and 6 that the force acting on the walls predicted by the CT is given by²⁸

$$F = \pi\gamma ah \frac{1 - a \sin(\theta)}{(1 - a^2)u(a, 1)} \quad (7)$$

For $\theta > 90^\circ$, eqs 6 and 7 are formally valid but the elliptical integrals $u(a, 1)$ and $\sigma(a, 1)$ have a different form, given by eqs S31 and S32 of the Supporting Information of ref 11.

We note that eq 7 is equivalent to the more familiar expressions for the force on the walls that can be obtained from basic classical mechanics (and the definition of surface tension)¹

$$F = 2\pi r_b \gamma \sin \theta - 2\pi r_b^2 \gamma H \quad (8)$$

and

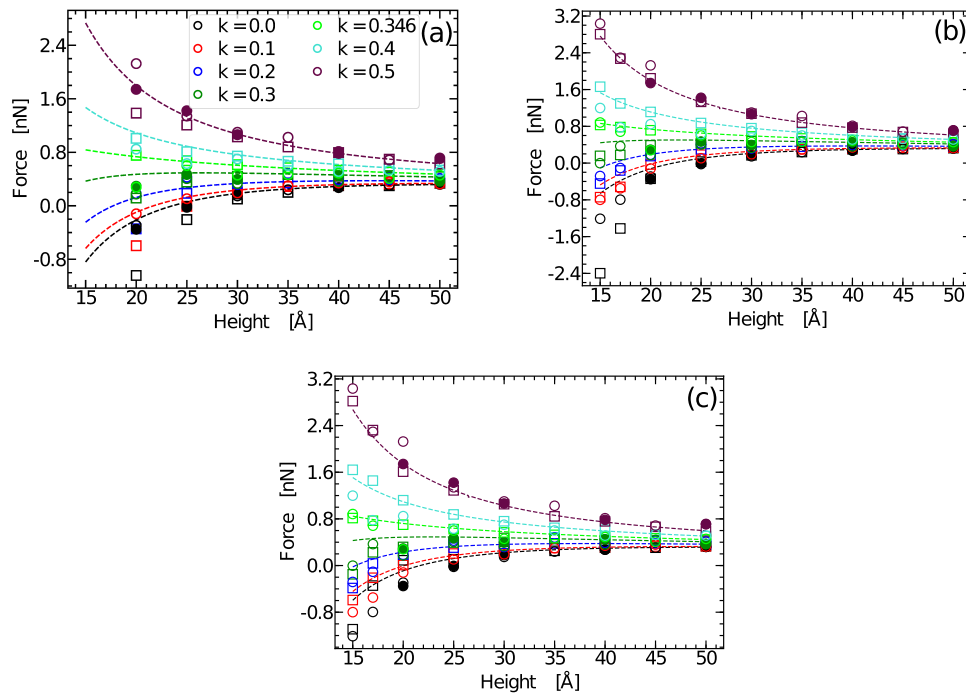


Figure 8. Forces induced by the WCB on the walls as a function of the wall separation h and for all surface polarities k studied. Circles are the forces measured from the MD simulations. Squares and dashed lines are, respectively, the predictions from the CT using eqs 7 and 8 where contributions from the line tension are neglected. The forces calculated from the MD simulations are consistent with the predictions from the CT down to $h \approx 25 \text{ \AA}$ for all surfaces considered (contributions from the line tension being omitted). Error bars are smaller than the symbol sizes. Panels (a), (b), and (c) are based on different methods used to calculate the WCB from MD simulations and correspond to Figures 8a, 8b, 8c, respectively.

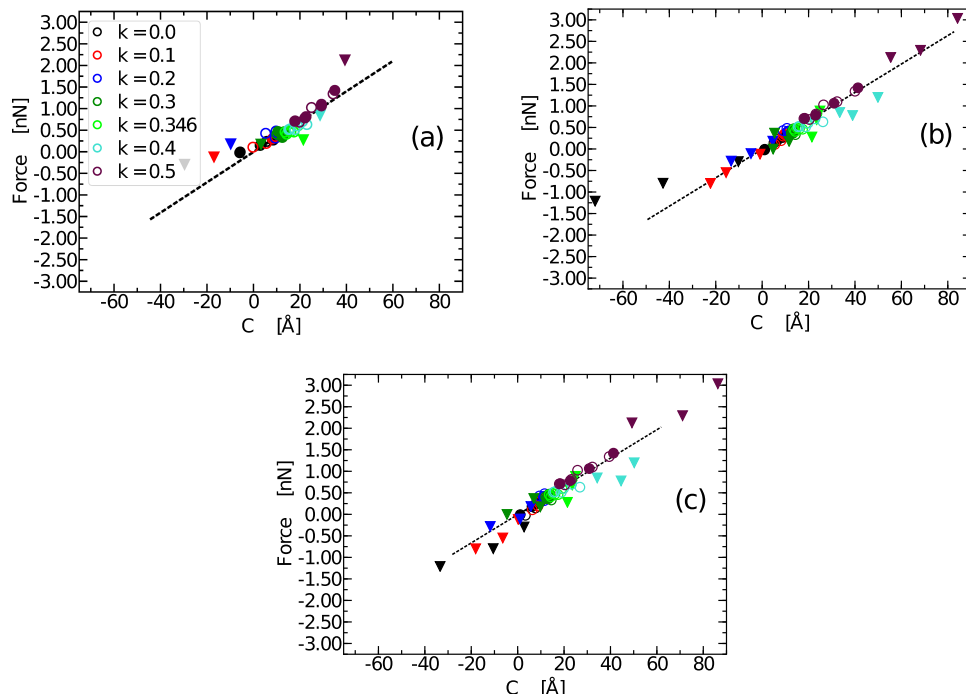


Figure 9. Forces induced by water capillary bridges formed between parallel walls as a function of the neck parameter $C = r_0 - Hr_0^2$ for all surface polarities k . Circles and triangles correspond to wall separations $h \geq 25 \text{ \AA}$ and $h < 25 \text{ \AA}$, respectively. The black dashed line is the best linear regression intercepting the origin for $h \geq 25 \text{ \AA}$. The slope of this interpolating line is used to determine the surface tension γ ; see Table 8. Error bars are smaller than the symbol sizes. Panels (a), (b), and (c) are based on different methods used to calculate the WCB from MD simulations; see the text.

$$F = 2\pi r_0 \gamma - 2\pi r_0^2 \gamma H = 2\pi \gamma C \quad (9)$$

where $C = r_0 - Hr_0^2$ is a parameter that measures the deformation of the WCB neck.¹⁰

Figure 8a–c shows the forces measured directly from our MD simulations (circles). The corresponding predictions from the CT, with no contributions from the line tension, are given by **eqs 8**, squares, and **7**, dashed lines. The differences among **Figure 8a–c** are in the method used to calculate the profile of the WCB from MD simulations, which provides the parameters needed in **eq 8**. Specifically, in **Figure 8a**, the required parameters are taken from **Tables 1** and **2** (the WCB profiles are shown in **Figures 3** and **S1** of the Supporting Information and are obtained with $\delta_s = 5 \text{ \AA}$). Similarly, in **Figure 8b**, the CT forces are calculated using the parameters of **Tables S1 and S2** of the Supporting Information (WCB profiles are shown in **Figure S7** of the Supporting Information and are obtained with $\delta_s = 2.5 \text{ \AA}$ after removing one point of $r_{\text{MD}}(z)$ closest to each wall). In **Figure 8c**, the required parameters to calculate the CT forces are taken from **Tables 4** and **5** (WCB profiles are shown in **Figures 5** and **S6** of the Supporting Information and are obtained with $\delta_s = 2.5 \text{ \AA}$ after removing two points of $r_{\text{MD}}(z)$ closest to each wall).

The main points of **Figure 8** are that, independent of the method used to calculate the WCB from MD simulations, (i) the CT theory predicts successfully the forces calculated from the MD simulations for approximately $h \geq 25\text{--}30 \text{ \AA}$ and, hence, (ii) that the role played by the line tension at these wall separations is not relevant for the determination of the force on the walls. Indeed, the circles, squares, and dashed lines in **Figure 8a–c** practically overlap for approximately $h \geq 25\text{--}30 \text{ \AA}$.

For approximately $h \leq 25 \text{ \AA}$, deviations can be observed between the MD results (circles) and the CT (squares and dashed lines). Such deviations are sensitive to the method considered and the surface polarity of the walls. For example, for $k = 0.0$, the circles and squares in **Figure 8a** do not overlap while they do overlap in **Figure 8c**. Instead, for $k = 0.4$, the circles and squares in **Figure 8a** overlap while they do not overlap in **Figure 8b,c**.

The values of γ used in **eqs 7** and **8** to calculate the forces from the CT are obtained from **eq 9**. Specifically, we first plot the forces obtained from MD simulations as a function of C in **Figure 9**. As predicted by the CT (**eq 9**), the data for approximately $h \geq 25\text{--}30 \text{ \AA}$ can be fitted by a straight line that passes through the origin. Following **eq 9**, the slope of this line is $2\pi\gamma$. The resulting values of γ are given in **Table 8**. These

Table 8. Surface Tension Calculated from **Figure 9 for $h \geq 25 \text{ \AA}$**

figure	$\gamma \text{ (N/m)}$
Figure 9a	0.056(0.001)
Figure 9b	0.053(0.001)
Figure 9c	0.052(0.001)

values vary only slightly with the specific method employed to calculate the profiles of the WCB, and they are consistent with the values obtained in our previous studies ($\gamma = 0.052\text{--}0.055$).^{10,11}

III.IV. On the Assumptions of the Capillarity Theory. It follows from our previous discussions that (i) the macroscopic CT is able to predict both the geometric (e.g., profile) and thermodynamic properties (forces on the walls) of the WCB down to $h = 30 \text{ \AA}$ without the need to include contributions from the line tension. For example, at these separations, the contact angle of water is constant. (ii) At approximately $h < 30 \text{ \AA}$,

\AA , the contact angle of water and forces on the walls obtained from MD simulations deviate from the predictions of the CT. Including a line tension does not necessarily correct such deviations. In particular, the value of the line tension can be sensitive to the methodology employed to calculate the WCB profile (i.e., it is an ill-defined quantity). A natural question is why results (i)–(ii) hold. This may help to extend our conclusions to liquids other than water.

To address this question, we include in **Figure 10** the density profiles of water $\rho(z)$ as a function of the position z along the WCB (density profiles for additional values of h and k are included in **Figure S9** of the Supporting Information). To calculate $\rho(z)$, for a given surface polarity and wall separation, we define a cylindrical volume within the WCB that extends from one wall to the other. The axis of the cylindrical volume passes through the center of mass of the WCB and its radius is small enough, so the liquid–vapor interface is excluded ($r < r_c$ with $r_c = r_0 - 5.0 \text{ \AA}$ for hydrophilic walls and $r_c = r_b - 5.0 \text{ \AA}$ for hydrophobic walls). The density profile $\rho(z)$ is calculated considering only those water molecules within the so defined cylindrical volume.

Figure 10 shows that for all surfaces studied, $\rho(z)$ exhibits oscillations next to the walls. This indicates that water molecules are arranged in layers in the proximity of the surfaces, which is the common case of nanoconfined liquids.^{8,17–19} The gray shaded regions in **Figure 10** highlight such oscillations in $\rho(z)$. The extension of these gray shaded regions from the walls is approximately $\Delta z = 10 \text{ \AA}$ for all values of k . It follows that Δz provides an estimation of the solid–liquid interface thickness.⁴⁰ Indeed, the value of $\rho(z)$ beyond the gray shaded regions in **Figure 10** is $\approx 1.0 \text{ g/cm}^3$, which corresponds to the density of bulk SPC/E water at $P = 0.1 \text{ MPa}$ and $T = 300 \text{ K}$. The main point of **Figure 10** is that at approximately $h > 30 \text{ \AA}$, where $\theta(h)$ is practically constant, the two solid–liquid interfaces (gray shaded regions) are well-separated and, hence, one can identify a volume of bulklike water within the WCB. Instead, at approximately $h < 30 \text{ \AA}$, where $\theta(h)$ varies with h , the two solid–liquid interfaces become very close to each other ($h = 25 \text{ \AA}$) or in contact with one another ($h = 20 \text{ \AA}$). Note that at $h = 25 \text{ \AA}$, the bulklike water represents a (cylindrical) slab of $< 5 \text{ \AA}$ thick while the water in the liquid–solid interfaces corresponds to two (cylindrical) slabs of 10 \AA thickness each. It follows that at $h < 30 \text{ \AA}$, there is a very small amount of water molecules, or no water molecules at all, that can be classified as bulklike (at $h < 25\text{--}30 \text{ \AA}$, less than $1/3$ of the water molecules can be classified as bulklike molecules). At roughly these separations, the water layers formed next to one of the walls start to interact with the water layers formed next to the opposite wall.

The CT assumes that the WCB can be considered to be composed of a volume of bulklike water enclosed by solid–liquid and liquid–vapor interfaces. It follows that the range of h at which $\theta(h)$ deviates from its asymptotic constant value, i.e., $h \leq 30 \text{ \AA}$, coincides approximately with the wall separations at which the basic hypothesis of the CT does not hold. In other words, our results suggest that, in reality, the CT does not fail to predict the behavior of our nanoscale WCB. It is just that the hypothesis assumed by the CT is not satisfied at approximately $h \leq 25\text{--}30 \text{ \AA}$ and, hence, the CT should have never been applied at these conditions.

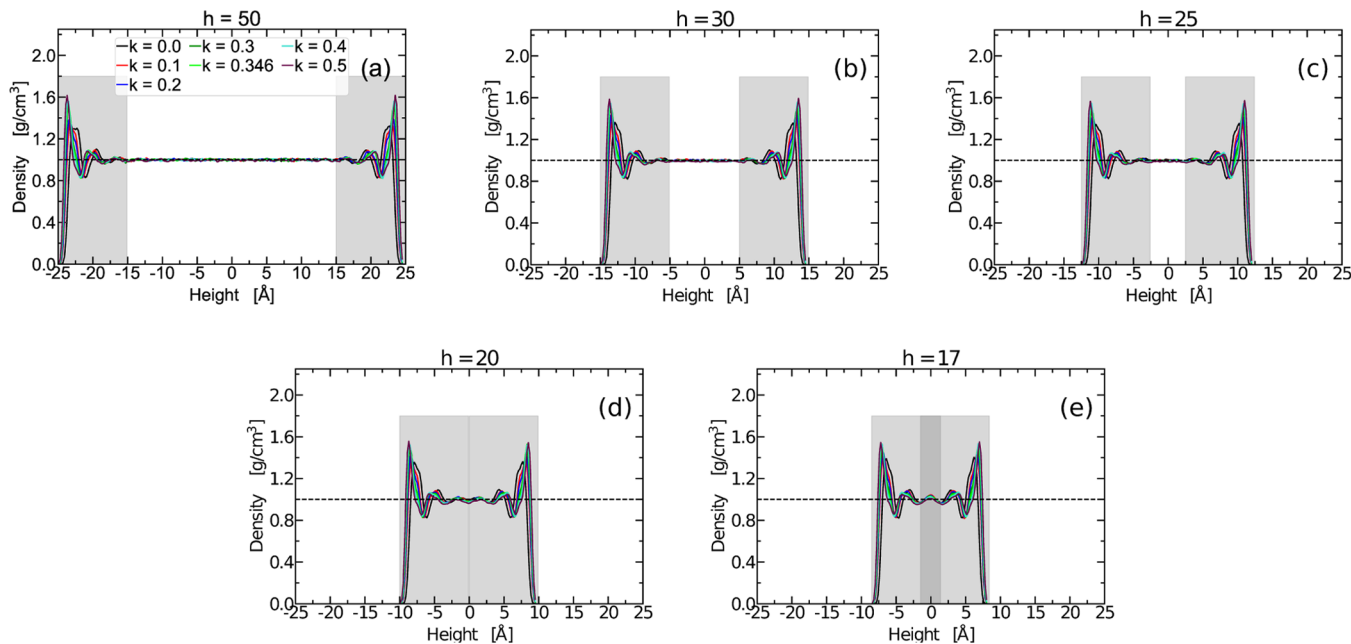


Figure 10. Density profile of water within the capillary bridge along the z -axis (perpendicular to the walls) for selected values of h and all surface polarities k studied (additional density profiles are included in Figure S9 of the Supporting Information). The gray regions expanding a distance $\Delta z \approx 10 \text{ \AA}$ mark the regions next to the walls where the density profiles show oscillation, i.e., where water molecules arrange into well-separated layers. Beyond these gray regions, the water density within the capillary bridge matches the density of bulk SPC/E water at $P = 0.1 \text{ MPa}$ and $T = 300 \text{ K}$ (dashed line). The CT assumes that the water bridge is composed of solid–liquid and vapor–liquid interfaces enclosing a volume of bulklike water. However, bulklike water is not found at $h \leq 20 \text{ \AA}$.

IV. CONCLUSIONS

We performed MD simulations of nanoscale WCB expanding between two identical walls separated by $15 \leq h \leq 50 \text{ \AA}$. Our main goal was to test the validity of the CT at the nanoscale using realistic water and wall models (the CT was originally proposed to describe the capillary phenomenon at $> 0.1\text{--}1.0 \mu\text{m}$ length scales). The surfaces considered are modeled based on silica (cristobalite) with surface charges tuned to generate hydrophobic and hydrophilic walls. We found that for $h > h_0 = 30 \text{ \AA}$, the CT works successfully for all surfaces considered, i.e., the CT was able to predict (i) the profiles of the WCB obtained from MD simulations and (ii) the forces induced by the WCB on the confining walls. In particular, we find that at these wall separations, the CT does not require the inclusion of a line tension.

At wall separations $h \leq h_0$, determining the profile of the WCB from MD simulations becomes problematic. The procedure followed to coarse-grain the density of the WCB from the snapshots obtained in MD simulations can lead to different qualitative results. For example, depending on how the WCB profile is calculated from the MD simulations, the contact angle of water $\theta(h)$ may be constant or it may vary with the wall separation. Since the CT, in its original formulation, predicts that $\theta(h)$ is independent of h , it follows that at $h \leq h_0$, one needs to take into consideration the role of the solid–liquid–vapor line tension when applying the CT. Since at these separations the WCB calculated from the MD simulations is sensitive to the method employed, the value of τ is also affected by the specific procedure followed to measure the WCB from the MD simulations. For example, our results show that values of τ can vary considerably depending on the method employed; e.g., in the case of our apolar surface ($k = 0.0$), the values of τ can be negative ($-0.00834 \times 10^{-9} \text{ N}$) or positive ($0.00011 \times 10^{-9} \text{ N}$). This is in contrast with the case

of water's liquid–vapor surface tension, γ ; in all cases, we find that $\gamma = 0.052\text{--}0.056 \text{ N/m}$, consistent with our previous studies.

That the breakdown of the CT occurs at the $O(1) \text{ nm}$ scale may not be surprising. After all, at approximately $\leq 10 \text{ \AA}$,¹⁴ water molecules confined by the walls studied here tend to arrange into layers parallel to the walls. The presence of such layers in the water structure is expected to give rise to oscillations in the forces induced on the confining walls (see, e.g., refs 17, 19, 41) indicating that at distances from the walls $\leq 10 \text{ \AA}$, water cannot be treated as a continuum, as assumed by the CT. What may be surprising from our results is that the CT fails already at about $h = 20 \text{ \AA}$, i.e., at wall separations at which the forces are still smooth functions of the wall separations. Indeed, we find that the forces remain monotonic functions of h for separations as small as $h = 15 \text{ \AA}$.

The CT assumes that the WCB can be considered to be a volume of bulklike water surrounded by liquid–vapor and liquid–solid interfaces. In this regard, our results are consistent with the density profile of water within the WCB studied. Specifically, the density profile of water indicates that for all hydrophobic/hydrophilic surfaces considered, the solid–liquid interface of water is $\approx 10 \text{ \AA}$ thick, comparable to the thickness of water's liquid–vapor interface.⁴⁰ Hence, at $h > h_0$, where the CT works successfully without including any line tension, there is a bulk-water slab within the WCB that is $\approx 10 \text{ \AA}$ thick. At $20 \text{ \AA} \leq h \leq h_0$, there are approximately $< 1/3$ of all water molecules that can be classified as bulklike. At $h < 20 \text{ \AA}$, where the CT breaks down (with or without including the line tension), the WCB is effectively an ‘interfacial film’ sandwiched between the confining walls with no bulklike water molecules within.

■ ASSOCIATED CONTENT

SI Supporting Information

The Supporting Information is available free of charge at <https://pubs.acs.org/doi/10.1021/acs.jpcc.0c11140>.

(i) Additional WCB profiles obtained at different conditions (h , k); (ii) additional results showing the sensitivity of the WCB profiles to technical details of the method employed (e.g., variations with δ_s); (iii) additional density profiles of water within the WCB for different values of h and k ; and (iv) proof for eq 3 (PDF)

■ AUTHOR INFORMATION

Corresponding Author

Nicolas Giovambattista — Department of Physics, Brooklyn College of the City University of New York, Brooklyn, New York 11210, United States; Ph.D. Programs in Chemistry and Physics, The Graduate Center of the City University of New York, New York 10016, United States; orcid.org/0000-0003-1149-0693; Email: ngiovambattista@brooklyn.cuny.edu

Authors

Alexandre B. Almeida — Instituto de Física, Universidade de São Paulo, São Paulo 05508-090, SP, Brazil

Sergey V. Buldyrev — Department of Physics, Yeshiva University, New York 10033, United States

Adriano M. Alencar — Instituto de Física, Universidade de São Paulo, São Paulo 05508-090, SP, Brazil; orcid.org/0000-0001-9324-2698

Complete contact information is available at:

<https://pubs.acs.org/10.1021/acs.jpcc.0c11140>

Notes

The authors declare no competing financial interest.

■ ACKNOWLEDGMENTS

The authors gratefully acknowledge support from FAPESP (São Paulo Research Foundation, Grant Number 2017/11631-2), Shell, and the ANP (Brazil's National Oil, Natural Gas and Biofuels Agency) through the R&D levy regulation. A.B.A. was supported by the Coordination for the Improvement of Higher Education Personnel (CAPES 88882.160170/2014-01). This work was supported, in part, by a grant of computer time from the City University of New York High Performance Computing Center under NSF Grants CNS-0855217, CNS-0958379, and ACI-1126113.

■ REFERENCES

- (1) de Gennes, P.; Brochard-Wyart, F.; Quéré, D. *Capillarity and Wetting Phenomena: Drops, Bubbles, Pearls, Waves*; Springer: New York, NY, 2004.
- (2) Rowlinson, J. S.; Widom, B. *Molecular Theory of Capillarity*; Dover Publications: Mineola, NY, 2013.
- (3) Laplace, P. S. *Supplement to Book 10 of Mecanique Celeste*; Crapelet, Courcier: Bachelier, Paris, 1806.
- (4) Young, T. An Essay on the Cohesion of Fluids. *Philos. Trans. R. Soc. London* **1805**, 95, 65–87.
- (5) Hu, D. L.; Chan, B.; Bush, J. W. M. The Hydrodynamics of Water Strider Locomotion. *Nature* **2003**, 424, 663–666.
- (6) Eichelsdoerfer, D. J.; Brown, K. A.; Mirkin, C. A. Capillary Bridge Rupture in Dip-pen Nanolithography. *Soft Matter* **2014**, 10, 5603–5608.

(7) Laube, J.; Salameh, S.; Kappl, M.; Mädler, L.; Ciacchi, L. C. Contact Forces between TiO₂ Nanoparticles Governed by an Interplay of Adsorbed Water Layers and Roughness. *Langmuir* **2015**, 31, 11288–11295.

(8) Giovambattista, N.; Rossky, P. J.; Debenedetti, P. G. Computational Studies of Pressure, Temperature, and Surface Effects on the Structure and Thermodynamics of Confined Water. *Annu. Rev. Phys. Chem.* **2012**, 63, 179–200.

(9) van Honschoten, J. V.; Brunets, N.; Tas, N. R. Capillarity at the Nanoscale. *Chem. Soc. Rev.* **2010**, 39, 1096–1114.

(10) Giovambattista, N.; Almeida, A. B.; Alencar, A. M.; Buldyrev, S. V. Validation of Capillarity Theory at the Nanometer Scale by Atomistic Computer Simulations of Water Droplets and Bridges in Contact with Hydrophobic and Hydrophilic Surfaces. *J. Phys. Chem. C* **2016**, 120, 1597–1608.

(11) Almeida, A. B.; Giovambattista, N.; Buldyrev, S. V.; Alencar, A. M. Validation of Capillarity Theory at the Nanometer Scale. II: Stability and Rupture of Water Capillary Bridges in Contact with Hydrophobic and Hydrophilic Surfaces. *J. Phys. Chem. C* **2018**, 122, 1556–1569.

(12) Tang, B.; Buldyrev, S. V.; Xu, L.; Giovambattista, N. Energy Stored in Nanoscale Water Capillary Bridges between Patchy Surfaces. *Langmuir* **2020**, 36, 7246–7251.

(13) Tang, B.; Yu, X.-J.; Buldyrev, S. V.; Giovambattista, N.; Xu, L.-M. Energy stored in nanoscale water capillary bridges formed between chemically heterogeneous surfaces with circular patches. *Chin. Phys. B* **2020**, 29, 114703.

(14) Giovambattista, N.; Rossky, P. J.; Debenedetti, P. G. Effect of Pressure on the Phase Behavior and Structure of Water Confined Between Nanoscale Hydrophobic and Hydrophilic Plates. *Phys. Rev. E* **2006**, 73, No. 041604.

(15) Giovambattista, N.; Rossky, P. J.; Debenedetti, P. G. Phase Transitions Induced by Nanoconfinement in Liquid Water. *Phys. Rev. Lett.* **2009**, 102, No. 050603.

(16) Gao, Z.; Giovambattista, N.; Sahin, O. Phase Diagram of Water Confined by Graphene. *Sci. Rep.* **2018**, 8, No. 6228.

(17) Valenzuela, G. E. Computer Simulation of the Effect of Wetting Conditions on the Solvation Force and Pull-Off Force of Water Confined between Two Flat Substrates. *J. Phys. Chem. C* **2018**, 123, 1252–1259.

(18) Li, T.-D.; Gao, J.; Szoszkiewicz, R.; Landman, U.; Riedo, E. Structured and Viscous Water in Subnanometer Gaps. *Phys. Rev. B* **2007**, 75, No. 115415.

(19) Cheng, S.; Robbins, M. O. Nanocapillary Adhesion between Parallel Plates. *Langmuir* **2016**, 32, 7788–7795.

(20) Lu, N.; Likos, W. J. Suction Stress Characteristic Curve for Unsaturated Soil. *J. Geotech. Geoenviron. Eng.* **2006**, 132, 131–142.

(21) Lu, N.; Wu, B. L.; Tan, C. P. Tensile strength characteristics of unsaturated sands. *J. Geotech. Geoenviron. Eng.* **2007**, 133, 144–154.

(22) Mitarai, N.; Nori, F. Wet Granular Materials. *Adv. Phys.* **2006**, 55, 1–45.

(23) German, R. M. *Liquid Phase Sintering*; Springer: New York, NY, 2013.

(24) Vitorino, M. V.; Vieira, A.; Marques, C. A.; Rodrigues, M. S. Direct Measurement of the Capillary Condensation Time of a Water Nanobridge. *Sci. Rep.* **2018**, 8, No. 13848.

(25) Kim, J.; Won, D.; Sung, B.; Jhe, W. Observation of Universal Solidification in the Elongated Water Nanomeniscus. *J. Phys. Chem. Lett.* **2014**, 5, 737–742.

(26) Jinesh, K. B.; Frenken, J. W. M. Capillary Condensation in Atomic Scale Friction: How Water Acts Like a Glue. *Phys. Rev. Lett.* **2006**, 96, No. 166103.

(27) Riedo, E.; Lévy, F.; Brune, H. Kinetics of Capillary Condensation in Nanoscopic Sliding Friction. *Phys. Rev. Lett.* **2002**, 88, No. 185505.

(28) Alencar, A. M.; Wolfe, E.; Buldyrev, S. V. Monte Carlo Simulation of Liquid Bridge Rupture: Application to Lung Physiology. *Phys. Rev. E* **2006**, 74, No. 026311.

- (29) Almeida, A. B.; Buldyrev, S. V.; Alencar, A. M. Crackling Sound Generation During the Formation of Liquid Bridges: A Lattice Gas Model. *Phys. A* **2013**, *392*, 3409–3416.
- (30) Plimpton, S. Fast Parallel Algorithms for Short-Range Molecular Dynamics. *J. Comput. Phys.* **1995**, *117*, 1–19.
- (31) Hockney, R. W.; Eastwood, J. W. *Computer Simulation Using Particles*; Taylor & Francis Group: New York, NY, 1988.
- (32) Berendsen, H. J. C.; Grigera, J. R.; Stroatsma, T. P. The Missing Term in Effective Pair Potentials. *J. Phys. Chem. A* **1987**, *91*, 6269–6271.
- (33) Xu, L.; Lio, A.; Hu, J.; Ogletree, D. F.; Salmeron, M. Wetting and Capillary Phenomena of Water on Mica. *J. Phys. Chem. B* **1998**, *102*, 540–548.
- (34) He, M.; Szuchmacher Blum, A.; Aston, D. E.; Buenaviaje, C.; Overney, R. M.; Luginbühl, R. Critical Phenomena of Water Bridges in Nanoasperity Contacts. *J. Chem. Phys.* **2001**, *114*, 1355.
- (35) Thundat, T.; Zheng, X.-Y.; Chen, G. Y.; Warmack, R. J. Role of Relative Humidity in Atomic Force Microscopy Imaging. *Surf. Sci. Lett.* **1993**, *294*, L939–L943.
- (36) Giovambattista, N.; Debenedetti, P. G.; Rossky, P. J. Effect of Surface Polarity on Water Contact Angle and Interfacial Hydration Structure. *J. Phys. Chem. B* **2007**, *111*, 9581–9587.
- (37) Werder, T.; Walther, J. H.; Jaffe, R. L.; Halicioglu, T.; Koumoutsakos, P. On the Water-Carbon Interaction for Use in Molecular Dynamics Simulations of Graphite and Carbon Nanotubes. *J. Phys. Chem. B* **2003**, *107*, 1345–1352.
- (38) Zangi, R.; Berne, B. J. Temperature Dependence of Dimerization and Dewetting of Large-Scale Hydrophobes: A Molecular Dynamics Study. *J. Phys. Chem. B* **2008**, *112*, 8634–8644.
- (39) The error ϵ is the square root of the average quadratic error between $r(z)$ and $r_{\text{MD}}(z)$, $\epsilon = \sqrt{\frac{1}{N_p} \sum_{i=1}^{N_p} d_i^2}$, where N_p is the number of points of $r_{\text{MD}}(z)$. See also refs 10, 11.
- (40) Romero-Vargas Castrillón, S.; Giovambattista, N.; Aksay, I. A.; Debenedetti, P. G. Evolution from Surface-Influenced to Bulk-Like Dynamics in Nanoscopically Confined Water. *J. Phys. Chem. B* **2009**, *113*, 7973–7976.
- (41) Engstler, J.; Giovambattista, N. Temperature Effects on Water-Mediated Interactions at the Nanoscale. *J. Phys. Chem. B* **2018**, *122*, 8908–8920.